Miniaturized Impedance Flow Cytometer: Design Rules and Integrated Readout

Marco Carminati **ID**, *Member, IEEE*, Giorgio Ferrari, *Member, IEEE*, Michael D. Vahey,
Joel Voldman, *Senior Member, IEEE*, and Marco Sampietro, *Member, IEEE*

Abstract—A dual-channel credit-card-sized impedance cell counter featuring a throughput of 2000 cell/s and detection of single yeast cells (5 μm) with a signal-to-noise ratio of 20 dB is presented. Its compactness is achieved by a CMOS ASIC combining a lock-in impedance demodulator with an oversampling 20-bit $\Sigma\Delta$ ADC and real-time peak detection embedded in field-programmable gate ar-ray. The module is coupled to a dielectrophoretic cell-sorting mi-crofluidic device, offering compact and label-free electrical readout that replaces the need for a fluorescence microscope and, thus, is suitable for point-of-care diagnostics. The independent role of each dimension of the planar sensing microelectrodes is demonstrated, with simulations and experiments, along with its relevant effect on the spectrum of thin channels, deriving useful design guidelines.

Index Terms—Dielectrophoretic cell separation, impedance flow cytometry, microfluidics, resistive pulse detection.

I. INTRODUCTION

One of the current challenges in the development and market affirmation of lab-on-a-chip (LOC) microsystems is the integration and miniaturization of all the components required for the operation of such chips at the point-of-care (POC), spanning from sample preparation to detection. In fact, despite two decades of development of microfluidics, today very often a "lab-around-the-chip", i.e., a complex setup consisting of bulky laboratory equipment such as microscopes, pumps, electromagnets [1] and bench-top electronic instruments (potentiostats, waveform generators, lock-in amplifiers), is still necessary to run the analysis. Clearly, microelectronics plays a pivotal role in this sense, enabling a radical miniaturization of several parallel channels of detection and processing circuits in millimetric chips, well matched with the miniaturization trends of microfluidics.

M. Carminati, G. Ferrari, and M. Sampietro are with the Dipartimento di Elettronica, Informazione e Bioingegneria, Politecnico di Milano, Milano 20133, Italy (e-mail: marco1.carminati@polimi.it; giorgio.ferrari@polimi.it; sampietr@elet.polimi.it).

M. D. Vahey is with the Department of Bioengineering and Biophysics Program, University of California, Berkeley, CA 94720 USA (e-mail: mvahey@berkeley.edu).

J. Voldman is with the Research Laboratory of Electronics, Massachusetts Institute of Technology, Cambridge, MA 02139-4307 USA (e-mail: voldman@mit.edu).

Color versions of one or more of the figures in this paper are available online at http://ieeexplore.ieee.org.

In order to address this relevant aspect, here we present a dual-channel credit-card-sized cell counter, based on a CMOS lock-in ASIC combined with a FPGA-embedded event counter. This module represents a viable example of a compact and really stand-alone detection system, where microfluidics, dielectrophoretic cell separation and microelectronics are combined. Furthermore, with the support of extensive experiments and numerical simulations, we derive design guidelines for optimal sizing of planar sensing electrodes and the height of the detection channel, whose role emerges, for the first time in this systematic study, as critical.

The employment of impedance for continuous-flow and high-throughput particle and cell detection in microfluidic devices (called *impedance flow cytometry*) has been spreading in the last decades and is now well consolidated [2], both with metal microelectrodes [3] and ionic "liquid electrodes" [4]. Representing an extension of the Coulter technique (resistive pulse sensing through a micro-pore obstructed by the translocating insulating body), the presence and the properties of a biological cell (with respect to the surrounding conductive medium) are probed as a perturbation of the electric field between a couple of adjacent electrodes [5]. The advantages of this fully electrical readout technique, with respect to optical detection, are: (i) absence of a fluorescent marker (no cell staining), (ii) compactness allowed by the absence of a microscope and lenses, (iii) direct compatibility with CMOS microelectronics [6], [7] and other electrochemical cell monitoring techniques [8], and (iv) margin for straightforward automation. Moreover, beyond counting and sizing, cell analysis and sorting based on electrical properties and phenotypes can be implemented [9]–[11]. Several enhancements have been reported targeting (i) higher throughput [12], (ii) smaller particle diameters [12], [13] and (iii) more robust event detection [14].

Despite the continuously-growing application of impedance detection in lab-on-a-chip microsystems, only a few papers have discussed the criteria for the design of the sensing electrodes. A complete analysis of the spectral impact of the configuration of facing electrodes (parallel plates on the top and bottom of the channel) was reported in [15]. For the case of coplanar electrodes (both on the channel bottom) some design rules were proposed in [16] although, as remarked in [17], the finite height of the microchannel was erroneously neglected. An optimal sizing criterion, experimentally demonstrated with a macroscopic setup, for facing electrodes has been obtained in [18], although not confirmed in the detailed analysis reported
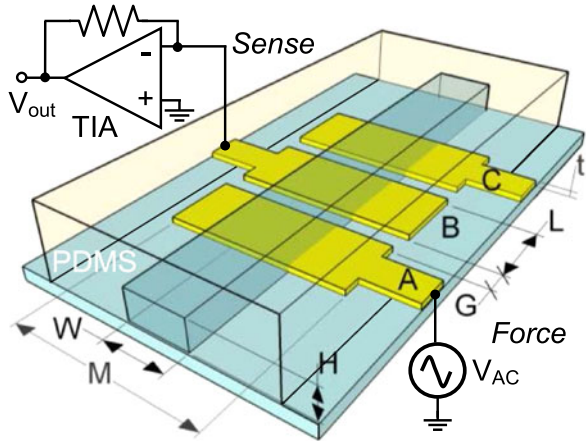
Fig. 1. Configuration of gold planar electrodes, patterned on a glass wafer bonded to a PDMS microchannel for impedance cell counting.

in [19] comparing numerically and experimentally the coplanar with the facing geometry.

The paper is organized as follows. Section II presents the design of the coplanar electrodes and channel, highlighting design guidelines. Section III illustrates the design of the electronic circuit, whose performances are experimentally characterized as reported in Section IV.

II. ELECTRODES DESIGN

The starting point of the system design are the sensing microelectrodes, on which the electronic readout is custom-tailored. A coplanar electrode geometry (see Fig. 1) is considered for its ease of fabrication (no top metallization, nor alignment required) and compatibility with hydrodynamic focusing solutions [20] avoiding the risk of channel clogging. Electrodes have a length L and are separated by a distance G. The total width is M, but the fraction in contact with the liquid corresponds to the width W of the microfluidic channel (of height H). The *force* electrode (A) is driven by a sinusoidal voltage (V_{AC} at frequency f_{AC}) and the current at the *sense* electrode (B) is amplified by a transimpedance amplifier (TIA) and demodulated by a synchronous lock-in detector (LIA). A third electrode (C) can be added to the single pair (A-B) for differential sensing, offering rejection to common-mode errors and drifts, which are significant for the ionic liquid, improving the signal-to-noise ratio (SNR) [21] and enabling particle velocimetry.

A. Resistive vs. Capacitive Detection

The ideal impedance between a couple of planar microelectrodes (A-B) in contact with an electrolytic solution is shown in Fig. 2(a) in dashed line. In the absence of Faradaic (redox) processes, the spectrum is characterized by three regions, corresponding to the three elements of the small-signal lumped model (inset). At low frequency the impedance is dominated by the capacitive nature of the metal/solution interface i.e., by the double layer capacitance (C_{DL}). For a standard physiological buffer solution (PBS, Phosphate Buffered Saline) it can be estimated through a specific capacitance of $0.1 - 0.2\,\mathrm{pF}/\mu\mathrm{m}^2$. Electrode

surface roughness, porosity and non-uniform distribution of time constants produce a pseudo-capacitive behavior, modeled by a constant-phase element (CPE) $Z_{CPE} = 1/(s \cdot C_Q)^n$ where C_Q is the pseudo-capacitance, whose value is frequency-dependent due to a sub-unitary exponent n (giving a slope of the impedance magnitude smaller than -20 dB/dec [22]).

As frequency increases, the impedance of C_{DL} is reduced and the solution resistance (R_{SOL}), given by the ionic resistivity ρ of the bulk solution ($\rho_{PBS} = 0.66\,\Omega\mathrm{m}$), becomes accessible. For a coplanar geometry, R_{SOL} can be calculated by means of conformal mapping [18]. At high frequency, the impedance is shunted by the parallel capacitance C_P. This capacitance is the sum of the geometric capacitance C_G, resulting from the dielectric material between the electrodes, and of the stray capacitance C_S, due to undesired stray couplings, for instance between the leads on the glass substrate and external connection wires. Temporarily neglecting the presence of C_S, we can calculate the cut-off frequency f_{cutoff}, above which the dielectric properties of the solution become accessible. This frequency is independent of the geometry of the electrodes (for parallel plate, coplanar and coaxial configurations) and is given by the inverse of the dielectric relaxation time, an intrinsic property of the solution: $f_{cutoff} = 1/(2\pi \varepsilon_0 \varepsilon_r \rho)$, where ε_r is the relative permittivity of the liquid (80 for water). In Fig. 2(b) the dependence of f_{cutoff} on the permittivity and resistivity of the solution is plotted. As shown (black dot), for PBS, f_{cutoff} is 330 MHz. Resistive detection is implemented measuring R_{SOL} below f_{cutoff}, while operating above it allows capacitive sensing of the particles and cells [23], [24]. From the point of view of the detection electronics, it is radically different to operate in the kHz-MHz range, where bridges and TIA/LIA are used, or in the GHz range, where microwave resonating circuits are necessary for capacitive detection [23]–[25]. For cell counting and sizing, the detection approach should be chosen according to the achievable sensitivity and to the compactness of the sensing circuitry. Considering the "contrast" i.e., the ratio between a given property (ε or ρ) of the cell with respect to the surrounding medium, it is evident that, for capacitive detection, the dielectric contrast is low (60 for cytoplasm vs. 78 for PBS) while, at low frequency, the single-shell model for biological cells [5] indicates a contrast in resistivity of orders of magnitude between the insulating cell membrane and the conductive medium. Consequently, resistive detection is chosen here.

B. Electrode Dimensions Optimization

The design of the electrodes has been led by two optimization criteria: (i) maximization of detection sensitivity (in terms of relative resistance variation $\Delta R/R$) and (ii) maximization of the width of the detection frequency range (i.e., of the resistive plateau in Fig. 2(a)). The latter is motivated by the interest in performing not only counting, but also discrimination of different cells types [10], [11].

The first parameter to be tuned is G, since it sets the vertical extension of the fringing electric field (95% of the field lines are confined within a height equal to G). Considering the range of diameters of the cells to be detected (in our case from the 5 μm
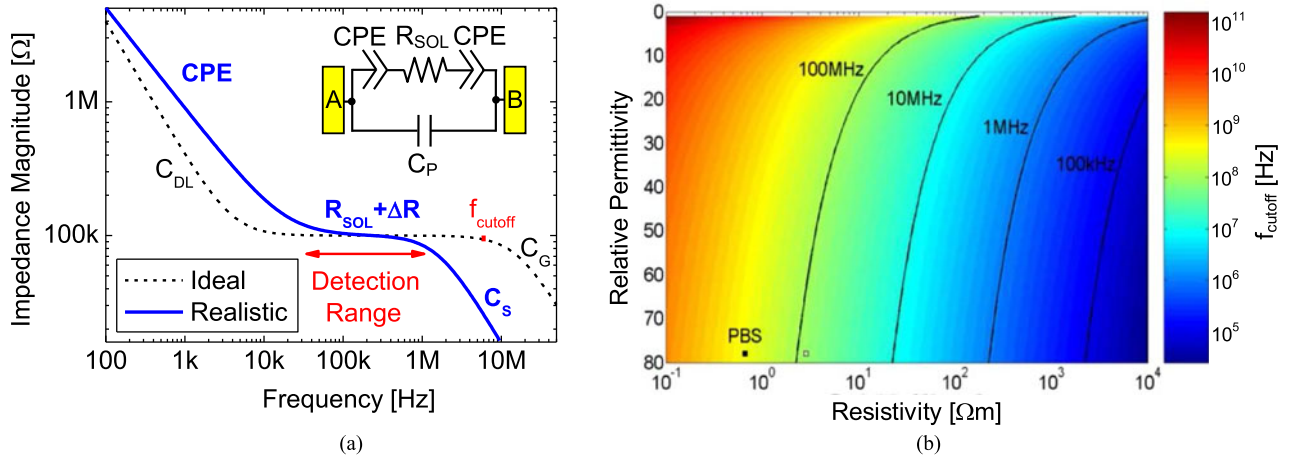
(a)

(b)

Fig. 2. (a) Ideal and actual impedance spectra simulated between a couple of coplanar electrodes: the solution resistance R_{SOL} is accessible in a narrow plateau limited at low frequency by the double layer capacitance C_{DL} and at high frequency by the stray capacitance C_S. (b) Map of the cutoff frequency value as a function of the medium electrical properties: resistivity ρ and relative dielectric constant ε_r. For physiological buffer medium (PBS) $f_{cutoff} = 330$ MHz.

(a)   (b)   (c)   (d)
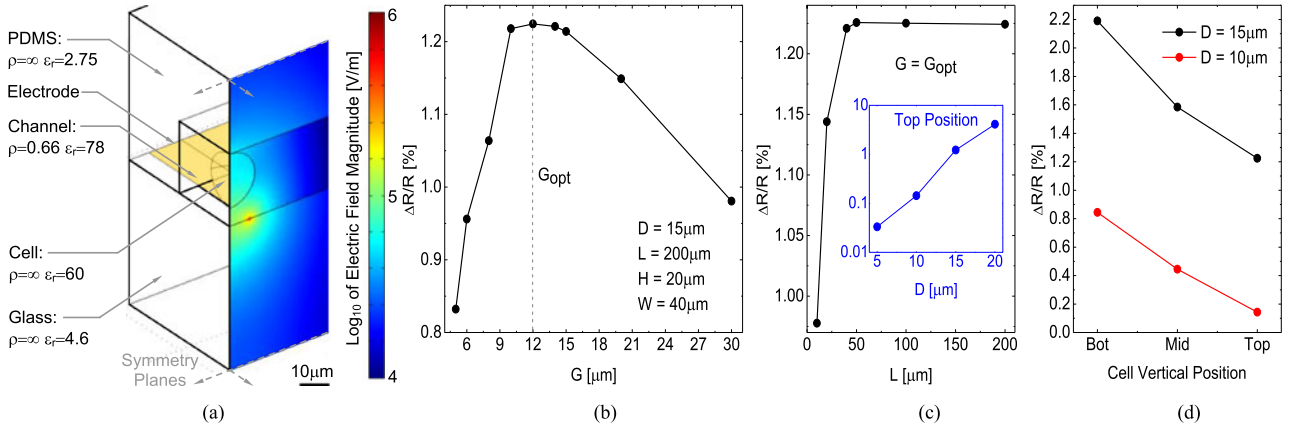
Fig. 3. (a) 3D COMSOL electrostatic simulations (quarter model) showing the relative resistance variation $\Delta R/R$ as a function of (b) the gap G, (c) the electrode length L and (d) of the cell height the channel (W = 2H = 40 μm). The inset shows the dependence on the cell diameter D which is cubic.

of yeast to 15 μm of mammalian cells), G will be sized close to the largest cell size. Finite-element numerical simulations have been employed to estimate $\Delta R/R$ and to finely tune the optimal value of G for a channel with W = 40 μm and H = 20 μm. A tridimensional simulation is required by the spherical shape of the cells but, thanks to the radial symmetry of the structure, only a quarter of the sensing volume [see Fig. 3(a)] has been simulated, thus saving memory and improving the accuracy. As reported in Fig. 3(b), simulations confirm that for a given cell size (15 μm), an optimal value G_{opt} exists (12 μm), which maximizes $\Delta R/R$ (1.2% variation of 25 kΩ resistance in the worst case). In fact, for G < G_{opt} the vertical penetration of the field is reduced below the position of the cell and the sensitive volume is shrunk. On the contrary, for G > G_{opt}, the sensitive volume is enlarged while the effect of the cell presence remains the same, thus reducing the volume fraction and correspondingly $\Delta R/R$.

Once the sensitive volume (i.e., G) has been matched with the cell volume to maximize the volume fraction modulation caused by the passing cells, the length of the electrodes and

the height of the channel can be chosen. As the electric field between the electrodes is dominated by fringe effects (the field magnitude at the edges is ~10 times higher than the average field between the edges as visible in Fig. 4), the value of L does not affect the value of R_{SOL} above a minimum length L_{min}. Simulations [see Fig. 3(c)] show that the charge on metal electrode extends only for the first tens of μm in the longitudinal direction and that for L > 50 μm, $\Delta R/R$ remains constant to the maximum value. This means that above L_{min}, L can be chosen independently of G. Very interestingly, if we consider the low frequency range, the double-layer electric field intensity is in the 100 MV/m range [26] along the whole metal-electrolyte interface. Thus, it is orders of magnitude higher than the average field in the gap due to V_{AC} in the middle-frequency range (2 V across 12 μm ~0.16 MV/m). Consequently, the whole length of the electrode contributes to C_{DL} (i.e., the impedance at low frequency), while only G and the first microns of L determine R_{SOL}. The cross-sectional simulations of Fig. 4 confirm this behavior: at low frequency (100 Hz), the field is constant in the double layer, while at high frequency (100 kHz) it van-
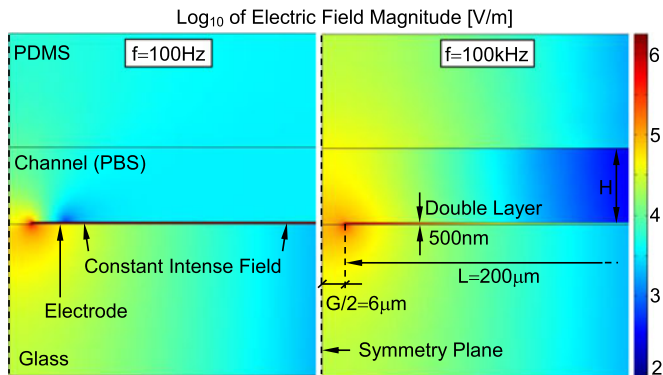
Fig. 4. 2D electric field simulations: the high field in the double layer region is evident at low frequency (left), while it rolls offs at high frequency (right).

Fig. 5. Triplets of coplanar electrodes (a) without and with the channel for (b) L = 200 μm, (c) L = 50 μm, (d) AFM image of the gap (G = 12 μm) and cross section (e) showing the gold thickness (with a roughness ~15 nm rms).

ishes across 50 μm. Differently from the simulations reported Fig. 3, focusing only on R_{SOL}, when the full spectrum is analyzed, the double layer must be simulated as well. The trick here adopted to combine a large simulation domain (tens of μm) with a non-meshable sub-nm double layer is to artificially thicken it (to 500 nm) and correspondingly increasing its ε_r (here to 5647).

The inset of Fig. 3(c) shows the cubic dependence of ΔR on the particle diameter D. Although much simpler to fabricate, the coplanar configuration suffers from a significant non uniformity of the vertical field, with respect to the parallel-plate geometry. Consequently, ΔR depends also on the vertical position of the cell h_{cell}, as shown in Fig. 3(d). Thus, vertical focusing (or more complex electrodes arrangements [27]) becomes important to eliminate this ambiguity (up to 50%), in order to be able to correlate ΔR with D for cell sizing.

C. Electrode Characterization

Electrodes are fabricated by means of lift-off lithography (thickness t = 200 nm of gold on 10 nm of Ti adhesion layer) on 6" Pyrex wafers to minimize the parasitics introduced by the substrate [28]. As reported in Fig. 5, G = 12 μm, M = 1 mm (for easy manual alignment of the PDMS channel), and two values of L: 200 μm [see Fig. 5(b)] and 50 μm [see Fig. 5(c)] are realized, in order to demonstrate the impact of this parameter.

In order to highlight the effect of the microchannel, the electrodes have been initially characterized in the absence of the channel. The area exposed to the liquid, limited with a thin PDMS gasket placed on the electrode chip [see Fig. 5(a)], is equal to M·L. The impedance spectra of uncovered electrodes are reported in Fig. 6. The impedance of dry electrodes has been measured to estimate the value of C_S, resulting 0.55 pF. Then, distilled water is added and the corresponding spectrum correctly shows three regions: the double layer one, the resistive plateau (corresponding to $\rho_{H_2O}^{-1} = 30$ S/cm) and a C_G = 2 pF. When water is replaced with PBS, the solution resistance is correctly reduced down to 330 Ω. The double layer region is best fitted by a CPE with exponent n = 0.89.

In order to demonstrate that the whole geometric area of the electrode in contact with the liquid contributes to the dou-
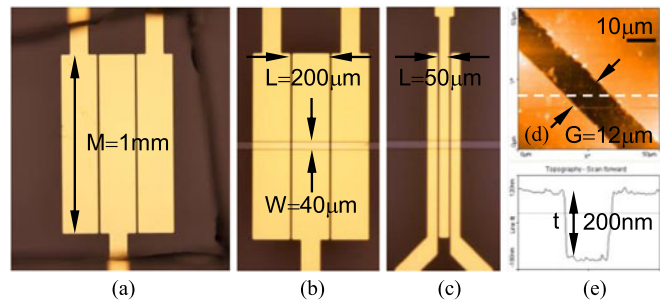
ble layer capacitance, two different measurement configurations have been compared: the coplanar vs. the vertical one. In the coplanar approach, the impedance is measured between a couple of planar electrodes (AB), applying the excitation potential to one electrode and reading the current from the other one. In this case two identical interfaces are in series. In the vertical approach, the impedance is measured between a single electrode of the triplet and a larger platinum counter electrode (CE) immerged in the PBS droplet from above. As CE is so macroscopic that it can be neglected, in this case a single interface is probed, resulting in a single C_{DL} in series to a higher R_{SOL} that is set by the distance between working and counter electrode. These measurements confirm that the whole electrode area contributes to the value of C_{DL}. In fact C_{DL} increases by a factor 4 when L increases from 50 to 200 μm, both in the vertical and in the coplanar sensing geometry. In all cases, the measured impedance is identical for the two adjacent couples (AB and BC), while R_{SOL} is higher for the AC case, where G is larger (~224 μm).

D. Impact of the Channel Height

Fig. 7 reports the spectra measured for the triplet of electrodes with L = 200 μm covered with a channel of H = 20 μm and W = 40 μm. The stray capacitance in dry conditions (0.5 pF) is correctly similar to value of the uncovered device. After filling the channel with buffer solution (in this case diluted PBS with $\sigma = 0.35$ S/m i.e $\rho = 2.85$ Ωm for DEP separation), the measured spectra show 4 different regions. Below 1 kHz, the double layer behavior is evident, with a CPE slope fitted by n = 0.8 (i.e., similar to the uncovered case). Between 100 kHz and 1 MHz the resistive plateau is visible, with a value $R_{SOL} = 100$ kΩ, in agreement with the estimations of conformal mapping (104 kΩ) and numerical simulations (108 kΩ). Above 1 MHz, the spectrum rolls off due to $C_S = 0.7$ pF. Very interestingly, between 1 kHz and 100 kHz, an unexpected *transition* region is visible, with a significantly smaller slope (n = 0.4). The change of slope occurring at 1 kHz is not described by the standard CPE + R_{SOL} model, adopted for thick channels, but is due to the confinement of the field lines caused by a thin channel. The effect of confinement is more evident for the A-C case, where the distance between the electrodes is larger. This inter-
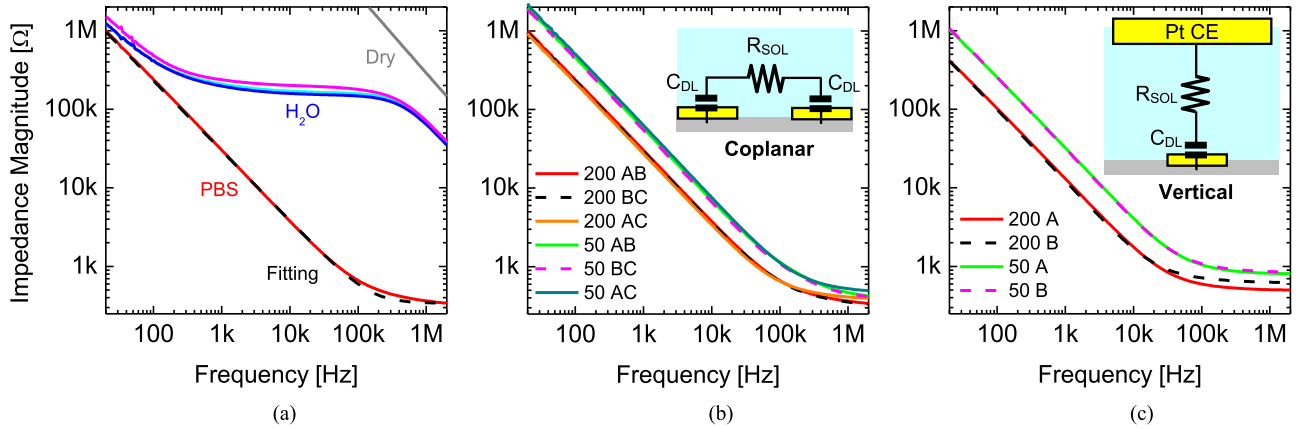
Fig. 6. Impedance spectroscopy preliminary characterization of electrodes in PBS without microchannel (as in Fig. 5(a)): (a-b) coplanar vs. (c) vertical sensing for different couples of electrodes (AB and BC with the same G = 12 μm, and AC with larger G) and values of L (50 and 200 μm). Measured spectra scale as expected.
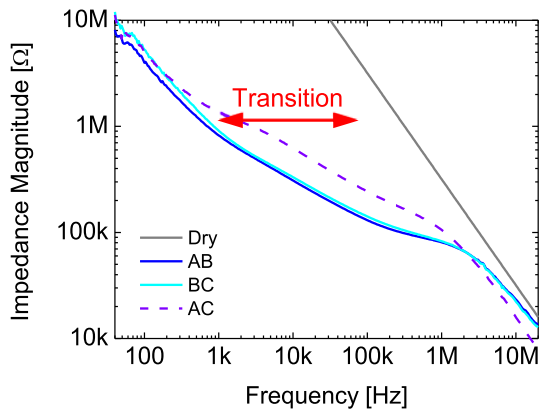

Fig. 7. Measured spectra of the electrodes covered with the channel (W = 2H = 40 μm) showing an unexpected −10 dB/dec. slope transition region (1–100 kHz) from the C_{DL} region to the R_{SOL} narrowing the resistive plateau.
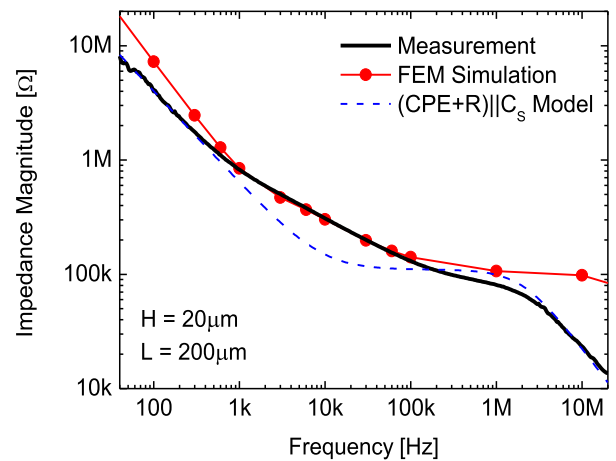

Fig. 8. Comparison of the measured impedance (black) with the conformal mapping mode [18] (dashed blue) and with the COMSOL simulation (red dots, Fig. 4) without C_S, showing excellent agreement in the transition region.

pretation of such an unexpected phenomenon is confirmed by COMSOL impedance simulations, performed in the same 2D domain shown in Fig. 4. As apparent in Fig. 8, the agreement between FEM simulations (red dots) and measurements (black line) is excellent in the transition region. Since in the simulation the external stray capacitance C_S and the CPE behavior of C_{DL} are absent, the resistive plateau remains flat up to 100 MHz and below 1 kHz and the slope is n = 1 instead of 0.8. The actual measured values of CPE and C_S are combined with the conformal mapping value of R_{SOL} into a simplified model (dashed blue) that accurately describes both capacitive ends of the spectrum.

Further comparative experiments have been carried out, characterizing devices with different geometrical parameters. In particular, as illustrated in Fig. 9, measuring the impedance of the same set of electrodes couples with a thicker channel (H = 30 μm, green), it is possible to see how the impedance increases and the transition are less evident. For the 30-μm thick channel, the slope in the transition remains the same also for
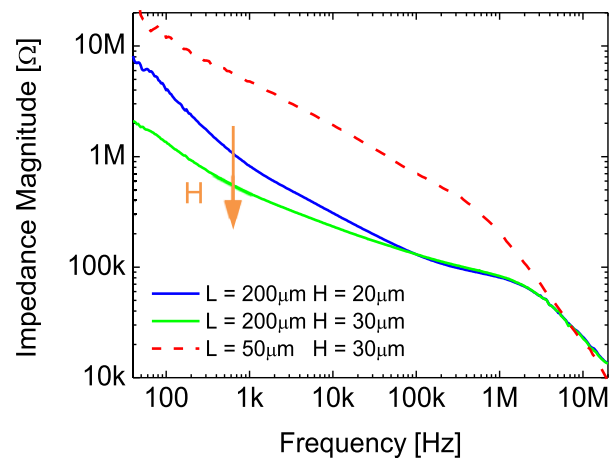

Fig. 9. Measured spectra for different channel heights (20 vs. 30) and L (50 vs. 200). The impact of the transition is less evident for a thicker channel.
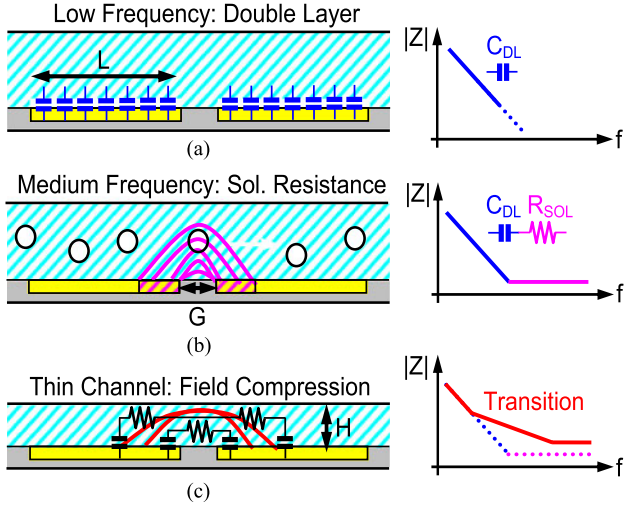
Fig. 10. Visualization of the relations between the geometrical dimensions: L (a), G (b) and H (c) and the spectrum region here demonstrated.

$L = 50 \, \mu m$ (dashed red), showing the independence of these two parameters.

Interestingly, several examples of this effect can be observed in the literature, although it is often overlooked and never pin-pointed. The transition slope is well evident for a channel with the same height of 30 μm [16], as well as down to 7 μm [3] and especially for nano-channels of 500 nm [29] in the wide frequency range from 50 Hz to 10 kHz for a solution of 10% PBS and 90% d.i. water.

E. Summary of Design Rules

As summarized in Fig. 10, separate spectral regions are controlled by different geometrical parameters. They can be set independently in order to maximize the performances:

1) L should be tuned to extend as much as possible the lower bound of the resistive plateau. It sets C_{DL} [see Fig. 10(a)]. By increasing L, C_{DL} increases, reducing the interfacial impedance at low frequency. Typically, with a fixed electrode geometry, this goal was achieved by increasing the effective electrode area, usually by increasing the surface roughness, for instance with Pt black treatment in the case of Pt electrodes [30].

2) G should be tuned to the optimal value that maximizes $\Delta R/R$. It sets R_{SOL} [see Fig. 10(b)]. Once L and G are chosen, the min. probing frequency f_{AC} is correspondingly set.

3) H should be reduced to align the cells against the sensing electrodes, but not too much, since a narrow channel (H < 3G) produces an impedance increase in the transition region [see Fig. 10(c)].

4) W can be adjusted to obtain the desired flow-rate Q, setting the transit time Δt and the measurement time.

5) Final rule: minimize the stray C_S (by tracks layout and connections setup, miniaturizing the readout) to extend the upped bound of the plateau, as well as to improve the noise performance of the TIA [31].
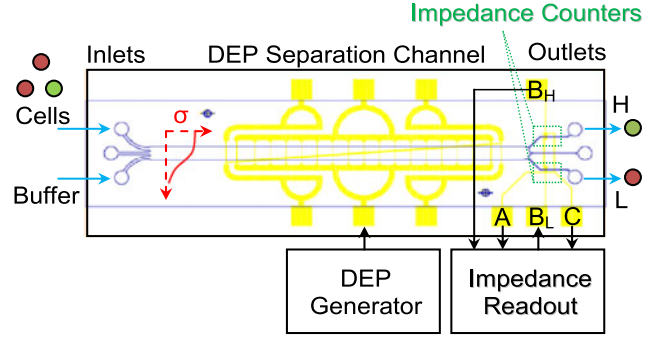

Fig. 11. Integration of two impedance cell counters at the outlets of an iso-dielectric cell sorter for label-free automatic operation.

III. DETECTION SYSTEM DESIGN

A. DEP Cell Sorter and Specifications

The impedance cell counters here designed are placed at the outlets of a label-free dielectrophoretic cell sorter [32] to replace fluorescence microscopy, thus making the system fully label-free. The iso-dielectric sorter (see Fig. 11), aimed at separating cells with similar size but different electrical phenotypes, such as healthy vs. dead or pathogenous or DNA-modified cells [33], [34], consists of a main large microfluidic channel (2 mm wide) where a conductivity gradient is created orthogonally to the flow direction, by means of two inlets (with high and low buffer conductivity) and an optional diffusive mixer. The inlets are fed by two syringes placed in a dual syringe pump, operating with flow rates in the μl/min range. Due to cell sedimentation, the syringe pump is kept in vertical position. A set of actuation electrodes (45 μm wide, spaced by 15 μm) running on the bottom of the separation channel with a 4° inclination with respect to it, generate a vertical negative-DEP barrier ($V_{DEP} = 4.5 \, V$). When a mixed population of cells or particles is loaded in the syringe and injected in the high-conductivity inlet, they experience repulsion and cannot cross the barrier. Thus, they are diagonally pushed by the hydrodynamic flow to slip toward lower conductivity regions. Consequently, they explore different surrounding properties until a zero net DEP force (iso-dielectric point) is reached and they can cross the barrier. Then, thanks to laminar flow, they continue to flow along a straight direction, as the only force acting on them is the pressure-driven hydrodynamic push. The iso-dielectric point differs for cells with different electrical properties, which get spatially separated. As shown in Fig. 11, the main channel splits at the end, after the separation is completed, into two output channels (width 40 μm) aimed at collecting separated populations. Thus, two identical cell counters are placed at both outlets, named H and L according to the conductivity level of the buffer. Three electrodes are placed below each output channel. The forcing electrodes (A and C for differential stimulation) are common to both channels, while the central sensing electrodes (B_H and B_L) have clearly separate connections to the electronic board where the device is plugged. They should be able to detect yeast and mammalian cells (diameter from 5 to 15 μm) at throughput in the 1000–10000 counts/s range (i.e., to be comparable with optical flow
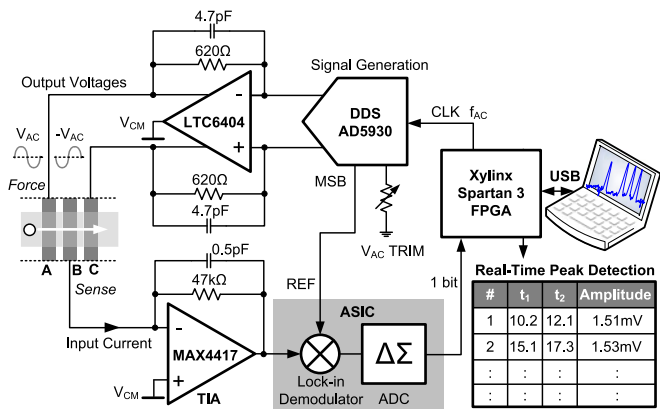
Fig. 12. Scheme of the cell counter circuit comprising a DDS sinusoidal differential generator ($+V_{AC}$ and $-V_{AC}$ at f_{AC}), a TIA input stage and an integrated lock-in demodulator and $\Sigma\Delta$ ADC connected to a FPGA.

cytometers [35]). A third middle inlet (and outlet) is visible in the blue PDMS mask of Fig. 11: it is meant for fluidic characterization purposes (no separation, no counting) when a single syringe is employed. In standard device operation, these ports are not opened (punched).

B. Circuit Design

The impedance measurement circuit is composed of two parts: a generation section, that produces the sinusoidal excitation waveform, and a current read-out and demodulation section, as illustrated in the scheme of Fig. 12. In order to achieve portability and fast throughput, personal computer-based elaboration has to be avoided due random delays and the prominent bottleneck of a limited data transfer rate. Thus, a local digital computing platform has been inserted for real-time smart impedance sensing: a field-programmable gate array (FPGA) has been selected for its abundant computational power, complete re-configurability and parallel elaboration capability.

The sinusoidal voltage signal necessary to probe the impedance in the plateau (from Fig. 8 from 100 kHz to 1 MHz) is generated by a dedicated off-the-shelf component (AD5930) based on the consolidated direct digital synthesis (DDS) technology. The frequency is directly set by the FPGA that provides, though a single digital line, a master trigger signal to which the generated frequency is locked. As normally the sinusoid amplitude is not adjusted during the measurement, but is set once at the beginning of the experiment, it can be manually regulated by means of a trimmer. In case computer regulation becomes necessary, the analog trimmer can be straightforwardly replaced by a digital potentiometer controlled via a digital bus. The trimmer sets the full scale range of the DDS whose differential output current is converted into a voltage by means of a fully-differential transimpedance stage (LTC6404). The sinusoid amplitude V_{AC} can be regulated from 10 mV to 1 V and the differential voltage excitation signal can be used for performing differential sensing with the triad of electrodes.

The current flowing across the channel, between the generation and the sensing electrode, is amplified and converted into a voltage by the transimpedance stage (MAX4417). In this

classical configuration, gain and bandwidth and noise are set by the value of the feedback resistor [31]. For the proper design of the analog stage, the equivalent model of Fig. 2(a) was adopted. A trade-off value of 47 kΩ was chosen. It sets a bandwidth of ~6 MHz, a gain of ~50 for differential signals and is characterized by a thermal noise comparable to the solution resistance ($R_{SOL-AB}||R_{SOL-BC} \sim 50$ kΩ).

In order to avoid any Faradaic current contribution due to electrochemical reactions at electrodes, all electrodes are biased at the same DC potential (indicated as V_{CM} in Fig. 12), set to the middle of the supply dynamic (1.65 V with respect the supply ground). This is the potential of the input virtual ground and the baseline of the sinusoidal signals (common mode voltage).

In order to track the 1% changes in the value of R_{SOL} f_{AC} is set in the 100 kHz-1 MHz range. For retrieving the impedance value, the output signal of the TIA is fed to a square-wave lock-in demodulator realized in a custom-designed ASIC (0.35 μm AMS CMOS process) and integrated with a 20-bit, 2nd order oversampling $\Sigma\Delta$ ADC [36]. Its single-bit output stream at 10 MHz is processed by the FGPA, where the low-pass digital filter (LPF) of the lock-in is implemented. An output sampling frequency of 20 kSa/s is chosen, corresponding to an over-sampling ratio of 2000, giving a SNR of the ADC better than 100 dB, i.e., negligible with respect to other noise contributions of the detector. The reference port of the mixer is supplied by the MSB output of the DDS, synchronous with f_{AC}.

The whole system is powered with a single 3.3 V supply regulated from the main 5 V line provided by the USB port. Due to the coexistence of analog and digital stages, special care has been devoted to power supply filtering, decoupling and to the layout (separate ground planes).

C. Real-Time FPGA Peak Detection

The main role of the FPGA is to handle the impedance measurement with high temporal resolution (100 MHz master system clock f_{clock}) providing fast impedance tracking and to implement in real-time peak detection. As the synchronous demodulation is performed by the integrated analog lock-in, the main FPGA tasks are the selection of the sinusoid frequency, the low-pass filtering of the 10 MHz digital bit-stream at the output the $\Delta\Sigma$ modulator and peak detection. The selectable decimation factor sets, at the same time, the temporal resolution (from 50 μs to 1 s) and the noise level (for instance 100 ms time resolution for 20 bits).

As shown in Fig. 13, two identical signal processing chains are implemented for both channels (H and L): the LPF is implemented with a tunable 3rd-order IIR filter (LPF_1). Then, high-pass filtering is inserted in order to remove the baseline and compare the high-passed pulses with a selectable threshold (Th). In order to be more robust with respect to noise fluctuations, a 10% hysteresis is adopted around the threshold for event detection. The high-pass filter (HPF) is implemented by subtracting a low-passed filtered (LPF_2) replica from the signal. Each time a rising edge exceeds the rising threshold, a counter is started (starting time T_i) in order to measure the time width (Δt) of the peak (i.e., the time-over-threshold) and the peak
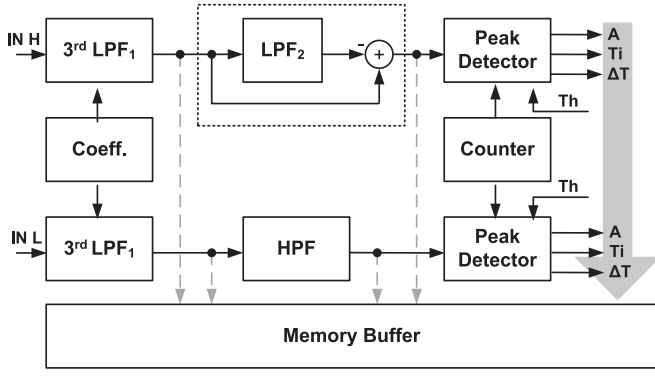
Fig. 13. Scheme of the FPGA firmware (identical for the two channels H and L): the digital stream coming from the lock-in/ADC is low-pass filtered (with selectable bandwidth LPF1), then high-pass filtered and then pulses undergo threshold-based (Th) peak detection. For each pulse, the stored data are amplitude (A), arrival time (T$_i$) and duration (ΔT) for both channels.
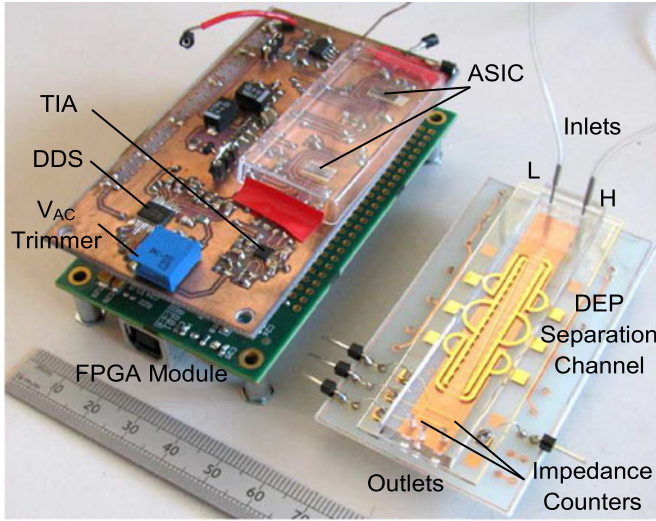

Fig. 14. Picture of the compact prototype (analog board coupled to an Opal Kelly FPGA module) matching the size of the DEP microfluidic sorter.

amplitude is calculated as the average of samples between the thresholds. These data are stored in a buffer memory for both independent and parallel channels and then transferred to a PC. For debugging purposes, intermediate signals can be saved as well. It has been experimentally found that minimum noise is achieved when f_{AC} is set equal to $f_{clock}/2^m$ (for any integer value of m). This is probably due to a better synchronization of the processing blocks inside the FPGA with the DDS, which avoids accumulating errors. Auxiliary tasks include the communication through a USB port with a laptop computer, used for setting the measurement parameters and storing the acquired data. A compact commercial module (XEM3010 by Opal Kelly, USA) integrating a Xylinx Spartan 3 FPGA, a PLL for clock generation, a USB bridge and RAM memory has been chosen.

IV. EXPERIMENTAL RESULTS

The compact cell counter (see Fig. 14) has been validated in four steps corresponding to increasingly complex setups: (i) with
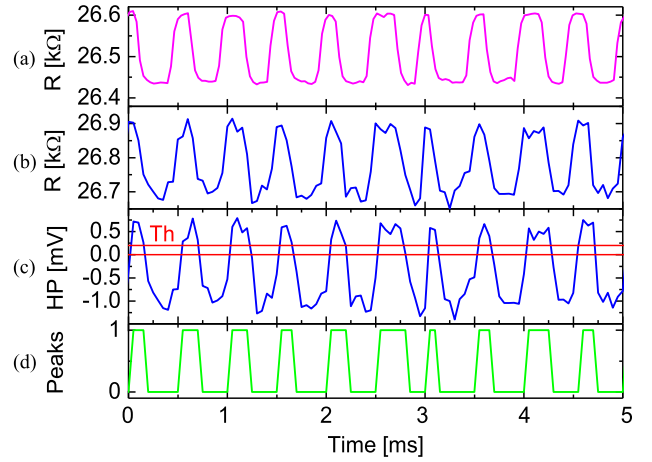

Fig. 15. Counter validation with a stream of $\Delta R/R = 0.75\%$ (a) output of a reference LIA (HF 2 LI by Zurich Instruments), (b) measured resistance by the counter, (c) high-passed signal with thresholds (in red), (d) stream of detected peaks. At 2000 count/s, the detection is error-free.

physical resistors modulated at high speed, (ii) with calibrated polystyrene beads, (iii) with yeast cells and (iv) during DEP separation of cells.

A. High-Throughput Assessment

First, in order to test the counting performance in a controlled way, a generator of dummy resistive pulses has been realized. It consists of a series of two physical resistors, one of which is shunted by a fast analog switch (ADG333), driven by a digital signal. The main resistor is chosen to match the value of R_{SOL} (30–100 kΩ depending on the medium), while the switched one is chosen to create the desired modulation ($\sim$1%). The switch is driven by an arbitrary waveform generator (with a sampling period of 15 μs), where the desired pattern of pulses, created in Matlab, is loaded. Several test sequences of pulses have been generated in Matlab with different distributions (uniform and Gaussian) of pulse durations (Δt) and inter-peak intervals. In this way, all the generated pulses have the same amplitude, while timings can be finely tuned. For synchronization purposes, a 1-second-long header is inserted at the beginning of each sequence, lasting several seconds and loop repeated. The whole test setup is shielded with a grounded metal box to reduce EMI pick-up.

The tracking performances of the system have been assessed in comparison with state-of-the-art instrumentation. As reported in Fig. 15, the same sequence of pulses ($\Delta R/R = 0.75\%$) at a rate of 2000 peaks/s has been tracked with a reference setup and with the proposed miniaturized cytometer. The reference setup is composed of a top-class bench-top LIA (HF 2 LI by Zurich Instruments, Switzerland) providing six demodulation channels and 50 MHz bandwidth, coupled with a low-noise variable-gain (10^5, 3.5 MHz bandwidth) TIA (DHCPA-100 by Femto, Germany) as a current front-end. This LIA is widely employed for impedance flow cytometry [27], [37], [38]. The excitation voltage (200 mV) and the sampling rate (20 kSa/s for the miniaturized counter and 28.8 kSa/s for the HF 2 LI)
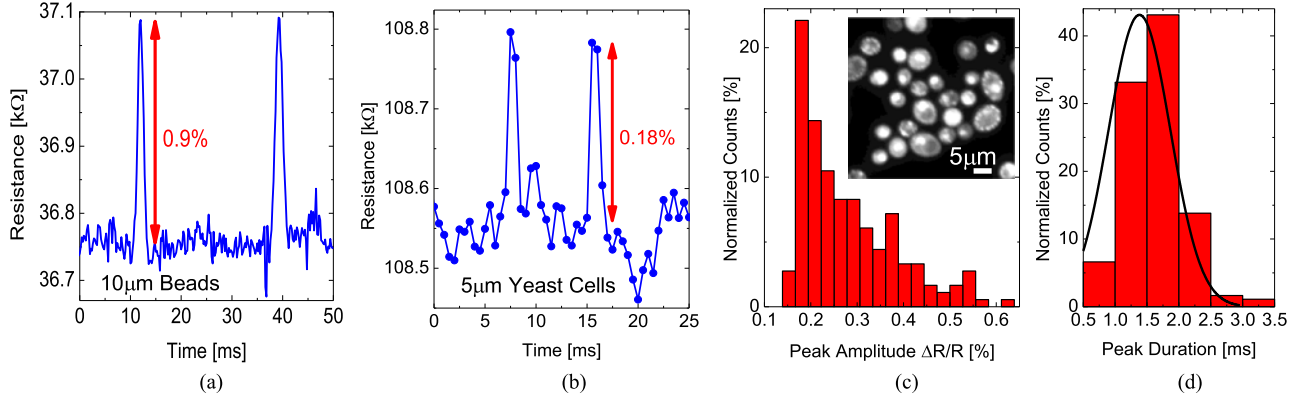
Fig. 16. Detection of (a) 10 μm polystere beads, of (b) yeast cells whose statitic distrubtions of (c) sizes and (d) travel times are in agreement with expectations.

are the same for both setups. As visible in Fig. 15, the SNR of the miniaturized counter is 19 dB [see Fig. 15(b)], smaller than 32 dB achieved by the HF 2 LI [see Fig. 15(c)], but acceptable in this application.

The histogram of the measured pulse widths matches with the statistical distribution created in Matlab. In this case the means pulse duration is 200 μs (spaced by 300 μs) with a standard deviation of 50 μs. No events are lost [see Fig. 15(d)], confirming an error-free detection rate up to 2000 cells/s.

B. Single Beads and Cell Counting and Sizing

The readout circuit is initially coupled to a microfluidic device with a single channel. Preliminary test with polystyrene beads [see Fig. 16(a)] of calibrated diameter (10 μm) in PBS are performed, showing a $\Delta R/R = 0.9\% \pm 0.1\%$ (consistent with beads size distribution), an average pulse width Δt of 2 ms ± 0.2 ms at a rate of 50 cells/s (10^3 beads/ml). With the detection parameters ($V_{AC} = 50$ mV, $f_{AC} = 97.5$ kHz, $f_s = 5$ kSa/s), the detection SNR is 23.5 dB.

Then, yeast cells (*Saccharomyces Cerevisiae* strain BY474 of nominal diameter 5 μm) in diluted PBS ($\sigma = 0.35$ S/m) at a concentration of 10^5 cells/ml and flow rate of 2.7 μl/min (corresponding to an average of ~2 cells/s with a maximum of ~200 cells/s as shown in Fig. 16(b)) are used. As routinely done in flow cytometry, 1% BSA (Bovin Serum Albumin), a non-specific protein, is added in order to reduce cell clumping and sticking to the walls of the channel, without affecting the measurement results. As shown in Fig. 16, single yeast cells are clearly detected. They produce an average $\Delta R/R = 0.18\%$ which is consistent with the value obtained for 10 μm beads, scaled by the volumetric ratio (2^3). With the optimized detection parameters ($V_{AC} = 650$ mV, $f_{AC} = 97.5$ kHz, $f_s = 2$ kSa/s), the detection SNR is ~20 dB. The value of R_{SOL} at ~100 kHz is 108 kΩ, consistent with the PBS dilution factor (~3), numerical simulations and preliminary measurements (see Fig. 8). The cell count rate scales linearly with the channel flow rate Q: 2.5 cells/s for $Q = 3 \mu$l/min a both inlets, and 1.1 cells/s for $Q = 1.5 \mu$l/min.

Despite the nominal value of diameter, the distribution of the peak amplitudes [see Fig. 16(c)] shows a tail towards larger dimension. This is confirmed in the literature [39], as well as

from a microscope image of the heterogeneous yeast population (inset) including buddying cells, significantly larger than 5 μm. The distribution of peak durations [see Fig. 16(d)] is narrow and centered around 1.5 ms, which is consistent with the flow rate ($Q = 1.5 \mu$l/min) giving a cell speed of 3 cm/s.

C. Real-Time Counting in Combination With DEP Sorting

Finally, the counter is operated in a complete on-chip cell manipulation experiment, with both channels operating simultaneously together with the DEP sorter. A specific strain of diploid yeast cells (strain BY4743) of 10 μm nominal diameter is used here. Yeast cells are stained with a green fluorophore (Fluorescin FITC) and injected only in the H inlet. Fig. 17 reports the comparison between the microscope images (a-d) and the impedance signals (e-h) at both H and L outlets in four cases (i–iv) corresponding to four positions of the stream of cells across the channel W. In fact, by changing the DEP driving frequency f_{DEP}, the sign of the dielectrophoretic force can be controlled [38] since the real part of the Clausius-Mossotti factor for yeast cells is negative at low frequency and positive above a cross-over frequency defined as $f_{cross} = \sqrt{2} \cdot \sigma_{SOL}/(2\pi \cdot r_{cell} \cdot C_m)$ where σ_{SOL} is the buffer conductivity (0.35 S/m), r_{cell} is the radius of the cell (5 μm) and C_m is the cell membrane specific capacitance (~0.01 pF/μm^2). With these values, it results ~1.5 MHz.

Impedance count rates (~20 cells/s) are simply calculated taking the number of counted cells during time slots of 200 s. Optical count rates are computed from microscope image analysis, taking the integral of the fluorescent signal in each microscope frames.

In the first case (i), the DEP is OFF, thus the cells flow only in sector H, where they are injected. The optical signal in the sector L is zero, while impedance detects very rare events (~2%) of cells randomly diffusing towards outlet L. In case (ii) at 1.9 MHz DEP is ON ($V_{DEP} = 4.5$ V) and weakly positive: the nDEP barrier is not formed, but the cell stream starts to be shifted from H (90% of counts) to L (10% of counts). At 1 MHz, $f_{DEP} < f_{cross}$ so that the negative barrier is growing, producing a further shift: 60% in H and 40% of cells in L sector. When f_{DEP} is reduced down to 500 kHz (iv), the vertical extension of the negative barrier reaches H, steering all the cells towards
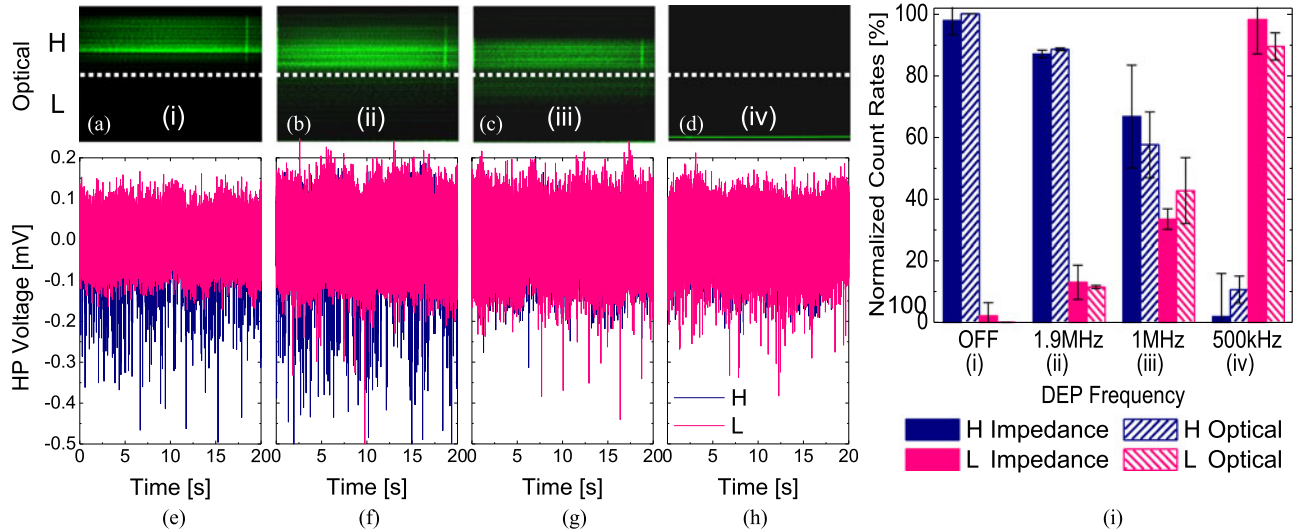
Fig. 17. Real-time impedance tracking of cells steered with DEP from the H to the L sector by changing the DEP frequency (i) to (iv), compared with microscope optical imaging (a–d). The normalized optical (a–d) and impedance (e–h) counts - simultaneously recorded - are in good agreement (m) in all conditions.

TABLE I
PERFORMANCE COMPARISON OF IMPEDANCE MICRO-CYTOMETERS

Ref.	Co.	W × H [μm^2]	D [μm]	SNR [dB]	f_{AC} [kHz]	BW [kHz]	T [s^{-1}]
This work	+ +	40 × 20	Beads 10 Yeast 5	23 20	100	10	2000
[41]	+	20 × 20 300 × 8	RBC 2.5 Beads 8	20 45	120	10	500
[42]	+	300 × 8 30 × 8	Beads 3 Beads 1	18 15	500	0.1	1.45
[43]	–	27 × 50	Beads 10	23	65	N.A.	N.A.
[44]	–	40 × 40	Beads 2.8	25	500	N.A.	N.A.
[14]	–	40 × 40	Beads 6	23	500	28	16

Co. is the compactness level of the readout electronics, W × H the cross-section, BW the detection bandwidth and T the reported throughput.

outlet L. In the latter case, the absolute count rate is lower since, by strong nDEP repulsion, all cells are pushed against the lateral wall of the channel (a thin aligned stream visible in the microscope image iv), thus experiencing larger friction. Furthermore, since they are pushed against the channel ceiling, i.e., far from the electrodes, the produced ΔR is smaller, but still well detectable.

Thanks to the lock-in spectral selectivity (provided that $f_{AC} \neq f_{DEP}$), no performance degradation is observed when the DEP section is activated. The good agreement between the impedance and optical fraction counts [see Fig. 17(m)] demonstrates the functionality of the designed dual-channel label-free cell counter, providing high-speed counting and sizing with granularity of single cells, impossible with optical microscopy.

V. CONCLUSIONS

The pervasive diffusion of microfluidic POC devices for personal healthcare and in-field biochemical monitoring is very often hindered by the limited portability of the auxiliary instrumentation required for the operation of LOCs. Impedance monitoring of cells, both in dynamic flow and in static cultures [8], allows replacing optical detection for label-free monitoring of the full cell cycle (including cytotoxicity and response to drugs [40]). Here we have presented the design of a high-performance (2000 cells/s throughput) dual-channel credit-card-sized impedance flow cytometer, starting from the design of the sensing electrodes, up to the characterization with yeast cells, manipulated by DEP. A synthetic comparison of the performances here demonstrated with respect to what offered by impedance flow cytometers recently reported in the literature [41]–[44] is shown in Table I. Note that only the first three implementations are actually featuring compact electronic readouts, while the remaining ones are based on bench-top LIAs.

In this work it has been experimentally demonstrated that, regardless of the fringe effects characterizing the strongly inhomogeneous field existing between coplanar electrodes, the whole geometric area of the electrodes contributes to the double layer capacitance C_{DL}, while the sensitivity to detect resistance variations due to passing cells is controlled by the electrode distance G. As a result, different geometric parameters of the microelectrodes can be sized independently. This independence is limited by the channel thickness: as H is reduced to increase the proximity of the cells with the sensitive layer, the resistive paths of ions are compressed, resulting in a non-linear increase of the distributed resistance that produces a second constant-phase behavior apparent as a further reduction in the impedance slope, unprecedentedly commented nor modeled in the literature.

Despite the combination of DEP separation with impedance flow cytometry on the same chip has been already reported [38], this is the first demonstration of operation of a compact readout system being really stand-alone and portable to the POC thanks to the combination with miniaturized integrated microelectronics and real-time FPGA processing.

References

[1] M. Monticelli *et al.*, "On-chip magnetic platform for single-particle manipulation with integrated electrical feedback," *Small*, vol. 12, no. 7, pp. 921–929, 2016.

[2] T. Sun and H. Morgan, "Single-cell microfluidic impedance cytometry: A review," *Microfluidics Nanofluidics*, vol. 8, pp. 423–443, 2010.

[3] H. E. Ayliffe, A. B. Frazier, and R. D. Rabbit, "Electric impedance spectroscopy using microchannels with integrated metal electrodes," *IEEE J. Micromech. Syst.*, vol. 8, no. 1, pp. 50–57, Mar. 1999.

[4] A. Valero, T. Braschler, and Ph. Renaud, "A unified approach to dielectric single cell analysis: Impedance and dielectrophoretic force spectroscopy," *Lab Chip*, vol. 10, pp. 2216–2225, 2010.

[5] M. Carminati, "Advances in high-resolution microscale impedance sensors," *J. Sensors*, vol. 2017, pp. 1–15, Mar. 2017.

[6] K. M. Lei, P. I. Mak, M. K. Law, and R. P. Martins, "CMOS biosensors for in vitro diagnosis - transducing mechanisms and applications," *Lab Chip*, vol. 16, no. 9, pp. 3664–3681, Sep. 2016.

[7] H. Li, X. Liu, L. Li, X. Mu, R. Genov, and A. J. Mason, "CMOS electrochemical instrumentation for biosensor microsystems: A review," *Sensors*, vol. 17, no. 74, pp. 1–26, Dec. 2016.

[8] M. Vergani *et al.*, "Multichannel bipotentiostat integrated with a microfluidic platform for electrochemical real-time monitoring of cell cultures," *IEEE Trans. Biomed. Circ. Syst.*, vol. 6, no. 5, pp. 498–507, Oct. 2012.

[9] S. Gawad, L. Schild, and Ph. Renaud, "Micromachined impedance spectroscopy flow cytometer for cell analysis and particle sizing," *Lab Chip*, vol. 1, pp. 76–82, 2001.

[10] D. Holmes *et al.*, "Leukocyte analysis and differentiation using high speed microfluidic single cell impedance cytometry," *Lab Chip*, vol. 9, pp. 2881–2889, 2009.

[11] R. Meissner, B. Eker, H. Kasi, A. Bertsch, and Ph. Renaud, "Distinguishing drug-induced minor morphological changes from major cellular damage via label-free impedimetric toxicity screening," *Lab Chip*, vol. 11, pp. 2352–2361, 2011.

[12] J. L. Fraikin, T. Teesalu, C.M. McKenney, E. Ruoslathi, and A.N. Cleland, "A high-throughput label-free nanoparticle analyser", *Nature Nanotechnol,*. vol. 6, pp. 308–313, 2011.

[13] C. Bernabini, D. Holmes, and H. Morgan, "Micro-impedance cytometry for detection and analysis of micron-sized particles and bacteria," *Lab Chip*, vol. 11, pp. 407–412, 2011.

[14] F. Caselli and P. Bisegna, "A simple and robust event-detection algorithm for single-cell impedance cytometry," *IEEE Trans. Biomed. Eng.*, vol. 63, no. 2, pp. 415–422, Feb. 2016.

[15] S. Gawad, K. Cheung, U. Seger, A. Bertsch, and Ph. Renaud, "Dielectric spectroscopy in a micromachined flow cytometer: Theroetical and practical considerations," *Lab Chip*, vol. 4, pp. 241–251, 2004.

[16] J. Hong *et al.*, "AC frequency characteristics of coplanar impedance sensors as design parameters," *Lab Chip*, vol. 5, pp. 270–279, 2005.

[17] P. Linderholm and Ph. Renaud, "Comment on 'AC frequency characteristics of coplanar impedance sensors as design parameters'," *Lab Chip*, vol. 5, pp. 1416–1417, 2005.

[18] P. Linderholm, U. Seger, and Ph. Renaud, "Analytical expression for electric field between two facing strip electrodes," *Electron. Lett.*, vol. 42, pp. 145–147, 2006.

[19] T. Sun, N.G. Green, S. Gawad, and H. Morgan, "Analytical electric field and sensitivity analysis for two microfluidic impedance cytometer designs," *IET Nanobiotechnol.*, vol. 1, pp. 69–79, 2007.

[20] R. Rodriguez-Trujillo, O. Castillo-Fernandez, M. Garrido, M. Arundell, A. Valencia, and G. Gomila, "High-speed particle detection in a micro-Coulter counter with two-dimensional adjustable aperture," *Biosensors Bioelectron.*, vol. 24, no. 2, pp. 290–296, 2008.

[21] M. Carminati, G. Gervasoni, M. Sampietro, and G. Ferrari, "Note: differential configurations for the mitigation of slow fluctuations limiting the resolution of digital lock-in amplifiers," *Rev. Sci. Instrum.*, vol. 87, no. 2, 2016, Art. no. 026102.

[22] C. M. Ionescu, J. A. Tenreiro Machado, and R. De Keyser, "Modeling of the lung impedance using a fractional-order ladder network with constant phase elements," *IEEE Trans. Biomed. Circuits Syst.*, vol. 5, no.1, pp. 83–89, Feb. 2011.

[23] G. A. Ferrier *et al.*, "Microfluidic electromanipulation with capacitive detection for the mechanical analysis of cells," *Biomicrofluidics*, vol. 2, 2008, Art. no. 044102.

[24] K. Mohammad and D. J. Thomson, "Differential ring oscillator based capacitance sensor for microfluidic applications," *IEEE Trans. Biomed. Circuits Syst.*, vol. 11, no.2, pp. 392–399, Apr. 2017.

[25] J. C. Chien and A. M. Niknejad, "Oscillator-based reactance sensors with injection locking for high-throughput flow cytometry using microwave dielectric spectroscopy," *IEEE J. Solid-State Circuit*, vol. 51, no. 2, pp. 457–472, Feb. 2016.

[26] R. Morrow, D. R. McKenzie, and M. M. M. Bilek, "The time dependent development of electric double-layers in saline solutions," *J. Phys. D*, vol. 39, pp. 937–943, 2006.

[27] D. Spencer, F. Caselli, P. Bisegna, and H. Morgan, "High accuracy particle analysis using sheathless microfluidic impedance cytometry," *Lab Chip*, vol. 16, pp. 2467–2473, 2016.

[28] M. Carminati, M. Vergani, G. Ferrari, L. Caranzi, M. Caironi, and M. Sampietro, "Accuracy and resolution limits in quartz and silicon substrates with microelectrodes for electrochemical biosensors," *Sensor Actuators B, Chem.*, vol. 174, pp. 168–175, 2012.

[29] N. F. Y. Durand and Ph. Renaud, "Label-free determination of protein-surface interaction kinetics by ionic conductance inside a nanochannel," *Lab Chip*, vol. 9, pp. 319–324, 2009.

[30] S. Zheng, M. Liu, and Y. C. Tai, "Micro coulter counters with platinum black electroplated electrodes for human blood cell sensing," *Biomed. Microdevices*, vol. 10, pp. 221–231, 2008.

[31] M. Crescentini, M. Bennati, M. Carminati, and M. Tartagni, "Noise limits of CMOS current interfaces for biosensors: a review," *IEEE Trans. Biomed. Circuits Syst.*, vol. 8, no. 2, pp. 278–292, Apr. 2014.

[32] M. D. Vahey and J. Voldman, "High-throughput cell and particle characterization using isodielectric separation," *Anal. Chem.*, vol. 81, no. 7, pp. 2446–2455, 2009.

[33] M. D. Vahey, L. Quiros Pesudo, J. P. Svensson, L. D. Samson, and J. Voldman, "Microfluidic genome-wide profiling of intrinsic electrical properties in saccharomyces cerevisiae," *Lab Chip*, vol. 13, no. 14, pp. 2754–2763, Jul. 2013.

[34] J. L. Prieto *et al.*, "Monitoring sepsis using electrical cell profiling," *Lab Chip*, vol. 16, pp. 4333–4340, 2016.

[35] B. Geheb *et al.*, "Low-noise, wide dynamic range sigma delta sensor interface with applications in microfluidic cell sorting," *IEEE Trans. Biomed. Circuits Syst.*, vol. 3, no. 3, pp. 1–11, Apr. 2009.

[36] F. Gozzini, G. Ferrari, and M. Sampietro, "An instrument-on-chip for impedance measurements on nanobiosensors with attofarad resolution," in *Proc. IEEE Int. Solid-State Circuits Conf.—Dig. Tech. Papers*, 2009, pp. 346–347.

[37] T. Lanz *et al.*, "Differential impedance spectrometer and vision system for analysis of single cells," in *Proc. Int. Solid-State Sensors, Actuators Microsyst. Conf.*, , 2009, pp. 1297–1300.

[38] G. Mernier, N. Piacentini, R. Tornay, N. Buffi, and P. Renaud, "Cell viability assessment by flow cytometry using yeast as cell model," *Sens. Actuat. B, Chem.*, vol. 154, no. 2, pp. 160–163, Jun. 2011.

[39] P. Palatt and G. Saidel, "Modeling and parameter estimation of yeast size distribution dynamics," *Ann.. Biomed. Eng.*, vol 7, no. 1, pp. 45–57, 1979.

[40] C. Caviglia *et al.*, "Impedimetric toxicity assay in microfluidics using free and liposome-encapsulated anticancer drugs," *Anal. Chem.*, vol. 87, no. 4, pp. 2204–2212, Feb. 2015.

[41] O. Castillo-Fernandez, R. Rodriguez-Trujillo, G. Gomila, and J. Samitier, "High-speed counting and sizing of cells in an impedance flow microcytometer with compact electronic instrumentation," *Microfluidics Nanofluidics*, vol. 16, no. 1/2, pp. 91–99, Jan. 2014.

[42] N. Talukder *et al.*, "A portable battery powered microfluidic impedance cytometer with smartphone readout: Towards personal health monitoring," *Biomed. Microdevices*, vol. 19, no. 36, pp. 1–15, Jun. 2017.

[43] M. Evander *et al.*, "Microfluidic impedance cytometer for platelet analysis," *Lab Chip*, vol. 13, pp. 722–729, 2013.

[44] S. Emaminejad, K.-H. Paik, V. Tabard-Cossa, and M. Javanmard, "Portable cytometry using microscale electronic sensing," *Sens. Actuators B, Chem.*, vol. 224, pp. 275–281, 2016.

Marco Carminati (M'07) was born in 1981. He received the B.Sc. and M.Sc. degrees (*summa cum laude*) in electronic engineering and Ph.D. degree in electronics from the Politecnico di Milano, Milan, Italy, in 2003, 2005, and 2009, respectively. He is currently an Assistant Professor with the Politecnico di Milano working in sensors, detectors, and low-noise electronics. He has authored more than 120 peer-reviewed international publications and holds one international patent.

Giorgio Ferrari (M'98) received the Laurea and Ph.D. degrees in electronics engineering from the Politecnico di Milano, Milan, Italy, in 1999 and 2003, respectively. Since 2005, he has been an Assistant Professor of electronics with the Politecnico di Milano. He has authored more than 100 journal and conference papers and seven book chapters and holds six patents.

Joel Voldman received the B.S. degree in electrical engineering *(summa cum laude)* from the University of Massachusetts Amherst, Amherst, MA, USA, in 1995, the Master degree in electrical engineering from the Massachusetts Institute of Technology (MIT), Cambridge, MA, USA, in 1997, and the Ph.D. degree from MIT in 2001. Since 2002, He has been member of MIT faculty, where he is an Associate Professor of electrical engineering and computer science since 2006.

Michael D. Vahey received the B.S. degree in electrical and computer engineering from Carnegie Mellon University, Pittsburgh, PA, USA, and the M.S. and Ph.D. degree from the Massachusetts Institute of Technology, Cambridge, MA, USA. He is currently a Postdoctoral scholar at the University of California, Berkeley, CA, USA.

Marco Sampietro was born in 1957. He received the M.S. degree in nuclear engineering from the Politecnico di Milano, Milan, Italy, in 1982. He is currently a Full Professor of electronic circuits and devices with the Politecnico di Milano. He is the Dean of the Bachelor and Master Course Program in Electronics Engineering at the Politecnico di Milano. He has coordinated several national and international projects and coauthored more than 200 peer-reviewed publications and holds five patents.